Dimensional crossover of quantum critical dynamics in many-body phase transitions

Qinpei Zheng ![ORCID],[1] Yuqing Wang ![ORCID],[2] Libo Liang,[1] Qi Huang,[1] Shuai Wang ![ORCID],[2] Wei Xiong,[1] Xiaoji Zhou,[1]
Wenlan Chen ![ORCID],[2,3,*] Xuzong Chen,[1,†] and Jiazhong Hu ![ORCID][2,3,‡]

[1]*School of Electronics, Peking University, Beijing 100871, China*
[2]*Department of Physics and State Key Laboratory of Low Dimensional Quantum Physics, Tsinghua University, Beijing 100084, China*
[3]*Frontier Science Center for Quantum Information and Collaborative Innovation Center of Quantum Matter, Beijing 100084, China*

The dimensional crossover induces varieties of quantum phenomena. In this paper, we demonstrate the quantum critical dynamics under dimensional crossover involving many-body phase transitions by continuously suppressing correlations and tunnelings along one direction of bulk materials, which provides a smooth connection from higher dimensions to lower ones based on the intrinsic correlations rather than geometry tailoring. By measuring the nonadiabatic excitations, the critical scaling laws in both three and two dimensions are observed and are consistent with predictions. In addition, we find scaling behaviors for intermediate regimes with noninteger dimensions. This study provides insights to extend the descriptions of critical exponents into more general or complex scenarios.

I. INTRODUCTION

One of the most important properties of a physical system is its dimension, and we observe a variety of novel phenomena in different dimensions [1–5]. While thinning a bulk material to a two-dimensional one, the reduced dimension also induces more exotic properties, such as the transition from Fermi liquid to Kondo physics [6], the enhanced thermal conductivity [7], and the swinging between abnormal Hall effects and topological Hall effects [8]. In addition, the dimension is also a critical exponent d describing quantum criticality [9–11], such as Josephson's identity [12,13], although most quantum critical phenomena can be described by universal scaling laws based on Landau symmetry breaking [11,14–23]. By changing the magnetic field or temperature, the critical scaling exponents can be changed from one set to another with different magnitudes and corresponding symmetries [24–28]. Therefore, it is intuitive and important to study what will happen when the dimension of a system changes, particularly when involved with quantum phase transitions, and what will change in the critical scaling laws, especially the critical exponents when the dimension cannot be integer-defined.

In previous research, the geometry of materials was changed to reduce the dimension [6–8,29–31] by thinning the layers of materials or cutting wires into points. However,

these approaches are mainly used on condensed-matter materials, and only steady properties such as transportation or magnetization are measured. In addition, it is not convenient to measure the dynamical or transient responses in the dimensional crossover region. It is also not clear how different dimensions are smoothly connected since the layers or unit cells must be integers with open boundaries.

On the other hand, we believe that the dimension of a system can also be decided by the correlations [17,32–37]. If we can strongly suppress the correlations or the dynamics along one direction of a three-dimensional system, the corresponding properties should be described by two-dimensional (2D) physics instead of three-dimensional (3D) physics. The 3D system will then be reduced into a series of independent layers of 2D systems. This provides a way to tune the dimension of a bulk material based on changing the correlations to smoothly connect a higher dimension to a lower one without influencing the integers of dimension and the boundary problems.

II. STEADY-STATE CALIBRATIONS

Here we utilize the unique tunability of ultracold-atom platforms to demonstrate a continuous dimensional crossover from a three-dimensional system to a two-dimensional one under many-body phase transitions, and we measure the dynamical response and the topological excitations during such nonadiabatic phase transitions. We observe a smooth crossover of critical scaling behaviors from 3D to 2D; although both scalings in 3D and 2D are consistent with previous predictions [9–11], the scaling in the crossover regime cannot be simply defined by the previous critical exponents. Upon further consideration of the bonding of all critical exponents, it indicates that the dimensional crossover continuously alters all other critical-scaling behaviors.

*cwlaser@ultracold.cn
†xuzongchen@pku.edu.cn
‡hujiazhong01@ultracold.cn

We prepare the Bose-Einstein condensates with $1.5(2) \times 10^5$ rubidium-87 atoms in $|F = 1, m_F = -1\rangle$ with a radius around 10 μm and load them into three-dimensional optical lattices. Each lattice beam is formed by reflecting the incident beam at the wavelength $\lambda = 1064$ nm with a beam waist of 150 μm at the atom position. We apply a magnetic field along the z-direction as the quantization axis, which is also the imaging direction. During the experiments, we keep the trap depths V_{xy} of the x-direction lattice and the y-direction lattice the same, but we may use a different trap depth V_z for the z-direction lattice. This provides an anisotropic Bose-Hubbard model,

$$H = -\sum_{m,n,q} \hat{b}_{m,n,q}^\dagger [t_{xy}(\hat{b}_{m-1,n,q} + \hat{b}_{m,n-1,q})$$
$$+ t_z \hat{b}_{m,n,q-1}] + \text{H.c.}$$
$$+ \frac{1}{2} \sum_{m,n,q} U \hat{n}_{m,n,q}^\dagger (\hat{n}_{m,n,q}^\dagger - 1), \tag{1}$$

where the subscripts m, n, and q label out the indices of the lattice sites along the x-, y-, and z-directions, and $\hat{n}_{m,n,q}^\dagger = \hat{b}_{m,n,q}^\dagger \hat{b}_{m,n,q}$ is the particle number operator. The coefficient t_{xy} corresponds to the tunneling amplitude in the x-y plane, and t_z corresponds to the tunneling amplitude along the z-direction.

Our measurement is based on the improved band-mapping method, which was demonstrated recently [22,23]. This improvement allows us to better distinguish the coherent part and the incoherent part in the optical lattices, with the coherent part corresponding to a sharp peak and the incoherent part exactly corresponding to a plateau in the first Brillouin zone. Based on this information, we extract out γ_{inc}, the fraction of the incoherent part in the atoms. This describes the phase coherence and correlations during the many-body phase transitions.

To show the influences of dimensions on the many-body critical dynamics, we first calibrate our systems with steady states. We ramp up the lattice depth adiabatically from 0 to the final values in 80 ms, in which the final values V_{xy} and V_z have different magnitudes. After reaching the final values, we hold the atoms at this stage for 20 ms, and then we apply the band-mapping [inset of Fig. 1(b)] to extract out the incoherent fraction γ_{inc}. In Fig. 1(a), we show the steady-state data of γ_{inc} versus V_{xy} and V_z. We see an overall trend in this plot that either increasing V_{xy} or V_z increases γ_{inc}. This suggests that the coherence between different sites is decreasing for larger trap depths in either of the directions. It is consistent with the intuition that the tunneling amplitudes, suppressed by large trap depths, push the systems into the Mott-insulator regime with less coherence. To more quantitatively analyze the observations, we compare the data by choosing a particular V_{xy} [Fig. 1(b)], such as $V_{xy} = 17E_r$. When V_z equals $17E_r$, the same as V_{xy}, the system is described by a three-dimensional Bose-Hubbard model. When V_z is increasing, t_z decreases stretched-exponentially. The tunneling amplitude t_z along the z-direction becomes 10 times smaller at $V_z = 30E_r$, and in this scenario the system should be described by several independent layers of two-dimensional optical lattices. Therefore, it realizes a continuous crossover from a three-dimensional
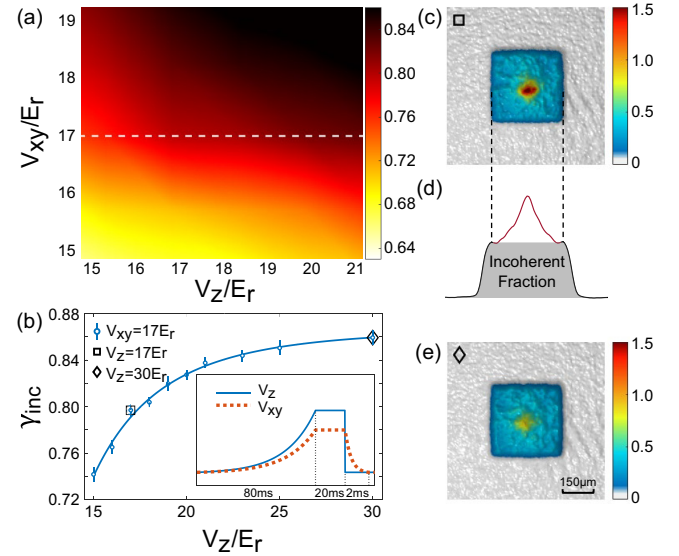
FIG. 1. The incoherent fraction for anisotropic optical lattices. (a) The incoherent fraction γ_{inc} vs the trap depth V_{xy} and V_z. The color bar from dark to light corresponds to the incoherent fraction from large to small. When γ_{inc} equals 1, the quasimomentum distribution is exactly a flat plateau. The dashed line is a label for the data shown in panel (b). (b) γ_{inc} vs V_z at $V_{xy} = 17E_r$ (blue circles with error bars of one standard deviation). The solid line is a fitting guideline. The square and the diamond correspond to the data with $V_z = 17E_r$ and $30E_r$, respectively, with their quasimomentum distribution in panels (c) and (e). The inset shows the ramping curves of V_{xy} and V_z. (c) The 2D quasimomentum distribution with $V_{xy} = V_z = 17E_r$. The color bar corresponds to the relative atomic density obtained from the absorption image along z. (d) The quasimomentum distribution along the y-direction by integrating the x-direction with $V_{xy} = V_z = 17E_r$. The plateau labeled by a gray shadow corresponds to the incoherent component, and the peak corresponds to the coherent component. The dashed line labels the first Brillouin zone. (e) The quasimomentum distribution with $V_{xy} = 17E_r$ and $V_z = 30E_r$.

Bose-Hubbard model to a two-dimensional one in a bulk material.

III. DYNAMICAL RESPONSE

To investigate the dynamics versus the system dimensions, we change the experimental procedure [bottom panel of Fig. 2(b)]. First we adiabatically load atoms into the lattices in 80 ms with $V_{xy} = V_i = 5E_r$ and a tunable V_z for different measurements, and then we hold the atoms for 20 ms. This stage prepares a superfluid sample with a tunable dimension depending on V_z. Then we ramp up V_{xy} linearly with a ramping speed k while V_z is kept unchanged. Once the trap depth reaches the final value, the band-mapping is applied to extract γ_{inc}. Compared with the measurement of steady states, the incoherent part fraction γ_{inc} is smaller than the value obtained in Fig. 1(a) due to the nonadiabatic dynamics, since some of the atoms cannot follow the external ramping immediately, which introduces excitations or topological defects in the systems. Then we use this difference $n_{ex} = \gamma_{inc}(\text{adiabatic}) - \gamma_{inc}(k)$ to characterize the excitation
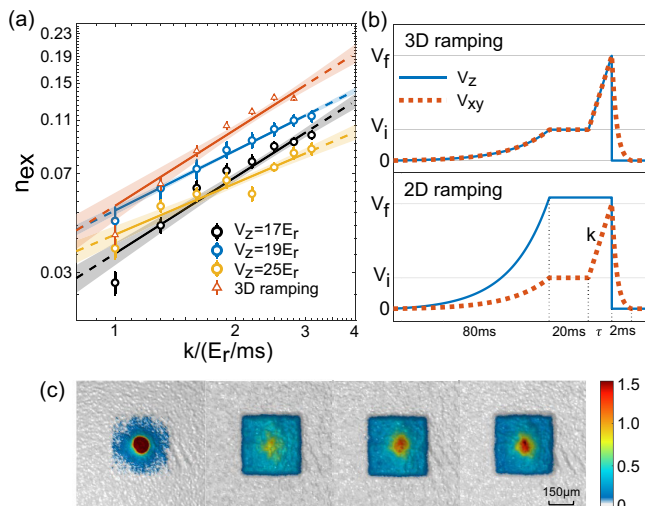
FIG. 2. The excitation vs the ramping. (a) Excitation fraction n_{ex} vs ramping speed, where n_{ex} characterizes the topological defects or excitation due to the nonadiabatic ramping. The detailed ramping protocol is shown in panel (b), where the black, blue, and yellow circles correspond to the data of the two-dimensional ramping with different fixed $V_z = 17E_r$, $19E_r$, and $25E_r$. The red triangles correspond to the data of the three-dimensional ramping. The solid lines are the fit of scaling laws $n_{ex} \propto k^\alpha$. The dashed lines are the extensions of fitting outside of the data range. Based on the fit, α equals 0.94(10), 0.74(4), and 0.63(9) for the 2D ramping with $V_z = 17$, 19, and $25E_r$, and α equals 0.93(11) for the 3D ramping. The error bars correspond to one standard deviation, and the shaded area corresponds to the 95% confidence interval of the fitting. (b) The ramping protocol of V_{xy} and V_z for the two-dimensional and three-dimensional schemes, where the horizontal axis is not plotted in scale. In both protocols, two gray lines correspond to the initial value V_i and the final value V_f of ramping. (c) The quasimomentum distribution. Left 1: the adiabatic states at $V_{xy} = 5E_r$, $V_z = 19E_r$; Left 2: the adiabatic states at $V_{xy} = 17E_r$, $V_z = 19E_r$; Left 3: the dynamical states at $k = 1.6E_r/ms$, $V_{xy} = V_f = 17E_r$, $V_z = 19E_r$; and Left 4: the dynamical states at $k = 3.1E_r/ms$, $V_{xy} = V_f = 17E_r$, $V_z = 19E_r$.

defects due to the nonadiabatic ramping. Intuitively, n_{ex} is proportional to the number of atoms that deviate from the steady states, and in the Appendix A we numerically prove the existence of this proportional relation in a superfluid and the shallow-Mott-insulator regimes.

This two-dimensional ramping characterizes the dynamics of phase transitions under different dimensions depending on V_z. When V_z equals $17E_r$, it is comparable to V_{xy} and the dynamics are still in the 3D regime. In Fig. 2(a), we show the data n_{ex} versus k for $V_z = 17E_r$. We fit them with a scaling law and obtain $n_{ex} \sim k^{0.94(10)}$. To compare with a real 3D case [upper panel of Fig. 2(b)], we measure the case of three-dimensional ramping and obtain a scaling as $n_{ex} \sim k^{0.93(11)}$, which is consistent with the two-dimensional ramping data at $V_z = 17E_r$. Then we measure the two-dimensional ramping at $V_z = 19E_r$ and $25E_r$ [Fig. 2(a)]. We find that all the data fall into the scaling relations $n_{ex} \sim k^\alpha$ but with different α, where α equals 0.74(4) and 0.63(9) for $V_z = 19E_r$ and $25E_r$, respectively. The tunneling amplitude t_z is 1.5 and 4.3 times smaller than the value at $17E_r$, respectively (inset of Fig. 4).

According to the theories of critical dynamics, the excitation defects have a scaling relation with k as [9–11,38,39],

$$n_{ex} \propto k^{\frac{d\nu}{1+\nu z}}, \qquad (2)$$

where for the mean-field treatment of the Bose-Hubbard model, we have the correlation exponent $\nu = 1/2$ and the dynamical exponent $z = 1$ for shallow Mott insulators with the particle-hole symmetry [10,11], and d is the system dimension. Therefore, n_{ex} is proportional to k^1 for the three-dimensional case and $k^{2/3}$ for the two-dimensional one. For our experiment, it is consistent that we observe $\alpha = 0.94(10)$ for $V_z = 17E_r$ (3D) and 0.63(9) for $V_z = 25E_r$ (2D).

To further understand how the two-dimensional and three-dimensional cases are connected, we follow the same protocol to measure n_{ex} versus the ramping speed k for different V_z. In Fig. 3, we choose different V_z for our measurement. For each of them, we ramp V_{xy} from $V_i = 5E_r$ to $V_f = 17E_r$ with a fixed V_z ranging from $17E_r$ to $30E_r$. In Fig. 3(b) we list out the data, which all fall into the fitting of $n_{ex} \sim k^\alpha$. Based on these, we obtain different α versus V_z. We find that α decreases from 1 to 2/3 when V_z increases, and once V_z is larger than $21E_r$, α approaches a steady value. There appears to be a smooth connection from 1 to 2/3 without any sudden jumps, but the exponent cannot be simply defined by integer dimensions according to Eq. (2). All the critical exponents are bounded by four identities (i.e., Rushbrooke, Widom, Fisher, and Josephson). Any changes in $d\nu$ will result in changes in other critical exponents. This suggests that the intermediate regime may have different critical scalings compared with the integer-dimensional systems, which we will leave for further experiments to explore.

IV. ESTIMATION OF CORRELATION LENGTHS

To give a more quantitative understanding from the theoretical side, we apply the Gutzwiller mean-field theory (GMFT) [40–42] to describe the ramping dynamics. Actually, the band mappings are performed in the shallow Mott-insulator regime, and the GMFT can still capture part of the actual physics. For each particular value of V_z, we ramp the trap depth V_{xy} along the x- and y-directions with a ramping speed k following the same protocol in experiments. Then, we calculate the incoherent part γ_{inc} and compare it with the value of the steady state to extract n_{ex}. The numerical results of n_{ex} versus the ramping speed k are shown as red squares in Fig. 3(b). Based on these, we extract the critical exponent α for different V_z. At $V_z = 15E_r$, α equals 0.95(5), which is the typical exponent predicted by critical dynamics theory in 3D systems [10,11], and α reaching 0.68(2) at $V_z = 28E_r$ describes the quasi-2D dynamics when $d = 2$ in Eq. (2). As V_z grows, the exponent goes down in a smooth trend in the same way as the experimental results, which shows similar behaviors of dimensional crossover in our systems [purple triangles in Fig. 3(a)].

We also want to understand why the third direction is suppressed in an anisotropic model. To better quantitatively characterize the spatial tunneling and correlations along this direction, we perform a quantum Monte Carlo method to calculate the Green function of the steady states,

$$G(i, j, \tau_1, \tau_2) = T_\tau \langle b_i^\dagger(\tau_1) b_j(\tau_2) \rangle. \qquad (3)$$
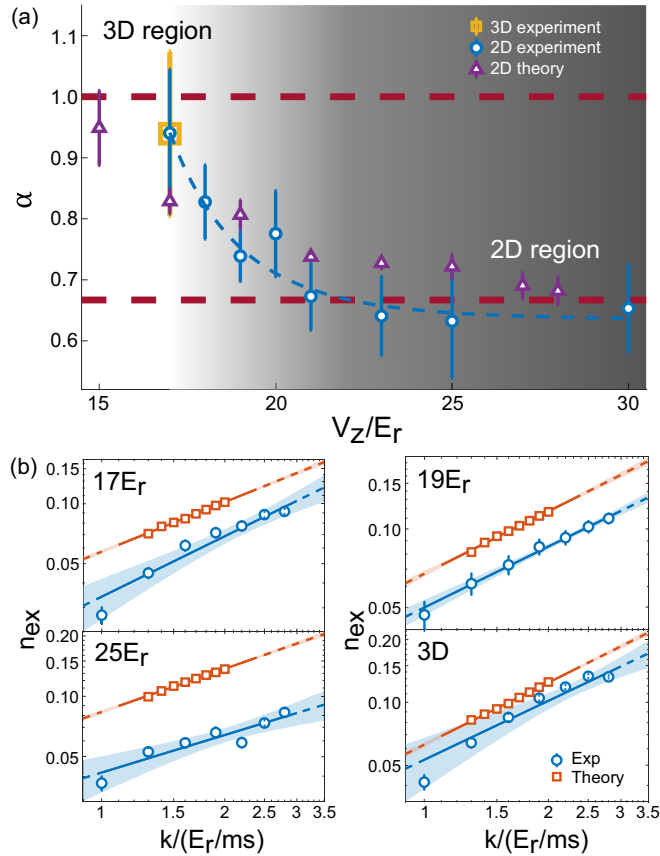
FIG. 3. The critical exponent α vs the third dimension suppression. (a) The critical exponent α vs the trap depth V_z of the third dimension. The hollow circles correspond to the experimentally obtained α by fitting $n_{ex} \propto k^\alpha$ for different V_z. The blue dashed line is a guideline of data. The purple triangles correspond to the critical exponent α under the 2D ramping calculated by the Gutzwiller mean-field theory. The yellow hollow square corresponds to the measured α for the 3D ramping. The theoretically predicted α for the 3D system is 1, while for the 2D systems it is 2/3, both marked by red dashed lines. (b) n_{ex} vs the ramping speed k for different V_z and 3D ramping procedures. The blue circles correspond to the measured data, and the red squares correspond to the calculation from the Gutzwiller mean-field theory. The solid lines are the fitting results. All the error bars correspond to the same standard deviation. The light-shaded areas correspond to a 95% fitting confidence interval.

To balance the consistency between the experimental parameters and the computational complexity, we simulate a $65\times65\times65$ anisotropic lattice with $3.3(1)\times10^3$ atoms by the worm algorithm [43,44]. The trap has the same geometry but the atom number is smaller. Since we are interested in the superfluid and the shallow-Mott-insulator regimes, fewer atoms can still capture the forming of $n = 1$ Mott insulators. Once the correlation length is much smaller than the size of the Mott insulators, it will not be affected by the finite-size effect. We calculate the effective normalized spatial correlation function along the z-axis as $G(z, \tau = 0) = \sum_{t,i} G(i, i + z, t, t)$ at $V_{xy} = 15E_r$ and we plot it in Fig. 4. The long-range transportation between sites decays with distance, hence $G(z, 0)$ obeys a stretched-exponentially decay with z [45], that is, $G(z, 0) = G_0 \exp(-b \times x^c)$. We extract out a distance ξ as
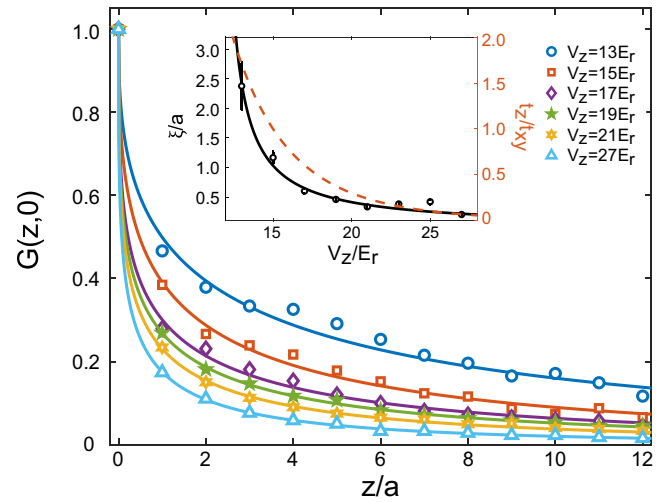
FIG. 4. Correlation functions along the z-direction. The main panel shows the Green functions vs distance z at $V_{xy} = 15E_r$. The colored dots are numerical results by QMC simulations for different V_z ranging from $13E_r$ to $27E_r$. The solid lines are obtained by fitting each set of dots with $G(z, 0) = G_0 \exp(-b \times z^c)$. The black solid line in the inset shows the correlation length ξ vs V_z. The correlation length ξ/a decreases smoothly from 2.4(4) to much less than 1. The error bars mainly come from fitting errors. The red dashed line indicates a downtrend of relative tunneling amplitude t_z/t_{xy} as V_z increases.

the correlation length when $G(z, 0)$ decays to $1/e$. When V_z increases from $13E_r$ to $27E_r$, ξ decreases from $2.4(4)a$ to $0.20(1)a$, where a is the lattice constant. This trend is consistent with the tunneling amplitude ratio t_z/t_{xy}, which decreases stretched-exponentially with V_z by more than tenfold. During the change of V_z, the interaction energy U only changes around 40% (see $U \sim V_z$ in the Appendix C) comparing with the exponential decay of t_z. At the region with more than one lattice constant, the correlation length provides a 3D configuration since the neighboring layered lattice is correlated, while at the $\xi/a < 0.5$ region or $t_z/t_{xy} < 0.2$, the correlations between nearby layers are suppressed, which induces the quasi-two-dimensional dynamics. However, the correlation length is a more fundamental reason for the dimensional crossover. If such a many-body system is interaction-free, it will be described by single-body physics and the correlation length will penetrate into all directions even for a very small ratio t_z/t_{xy}, where the existence of interaction suppresses the correlation length along the z-direction. Therefore, our simulation shows that dimensional crossover happens when the correlation length is exactly at one lattice constant in bulk materials, and only the monolayer of atoms may describe the real two-dimensional physics. More details of calculations can be found in the Appendix C.

V. CONCLUSION

In conclusion, we measure a continuous dimensional crossover from 3D to 2D in bulk materials by avoiding the influences of open boundaries. We observe the critical dynamics of quantum phase transitions with exponent scaling, and

we measure the critical exponents in the crossover region. We find that the critical exponents cannot be simply defined by the previously known values in systems with integer dimensions. Since the bonding of identity equations (Rushbrooke's, Widom's, Fisher's, and Josephson's) connects different critical exponents with a limited degree of freedom, our results show that other critical exponents in the crossover region also require further theoretical and experimental investigations.

APPENDIX A: GUTZWILLER MEAN-FIELD THEORY

In the main text, we adopt the Gutzwiller mean-field theory (GMFT) [40–42] to simulate the ramping dynamics of phase transitions in anisotropic optical lattices. Based on the method of GMFT, we write the many-body wave function $|\psi\rangle$ as a large product state between different lattice sites,

$$|\psi\rangle = \prod_i \left(\sum_n f_i^n |n, i\rangle \right), \tag{A1}$$

where each state $|n, i\rangle$ corresponds to n bosons occupying the lattice site with an index i, and f_i^n is the amplitude of this state. This assumption decouples the Hamiltonian, and we treat each site independently. Therefore, the Hamiltonian is converted into a mean-field form, which is

$$
\begin{aligned}
H_{\mathrm{MF}} = &- \sum_{m,n,q} \psi^*_{m,n,q}[t_{xy}(\hat{b}_{m-1,n,q} + \hat{b}_{m,n-1,q}) + t_z\hat{b}_{m,n,q-1}] \\
&- \sum_{m,n,q} \hat{b}^\dagger_{m,n,q}[t_{xy}(\psi_{m-1,n,q} + \psi_{m,n-1,q}) + t_z\psi_{m,n,q-1}] \\
&+ \sum_{m,n,q} \psi^*_{m,n,q}[t_{xy}(\psi_{m-1,n,q} + \psi_{m,n-1,q}) + t_z\psi_{m,n,q-1}] \\
&+ \mathrm{H.c.} \\
&+ \frac{1}{2}\sum_{m,n,q} U\hat{n}_{m,n,q}(\hat{n}_{m,n,q} - 1) \\
= &\sum_{m,n,q} h_{m,n,q}, \tag{A2}
\end{aligned}
$$

where t_{xy} or t_z are the tunneling amplitudes in the x-y plane or along the z-direction, respectively, and $\psi_{m,n,q} = \langle b_{m,n,q}\rangle$ is the mean value of the annihilation operator $b_{m,n,q}$, where m, n, q label the lattice site index along the x, y, and z directions, and $h_{m,n,q}$ is the mean-field Hamiltonian of site (m, n, q).

To prepare the equilibrium states with an ultracold temperature, we initialize the state with a random trial wave function and use the trial function to calculate the mean-field terms $\psi_{m,n,q}$. Based on these mean-field terms, we obtain the mean-field Hamiltonian and calculate the ground-state wave function. Then, we apply this ground-state wave function to
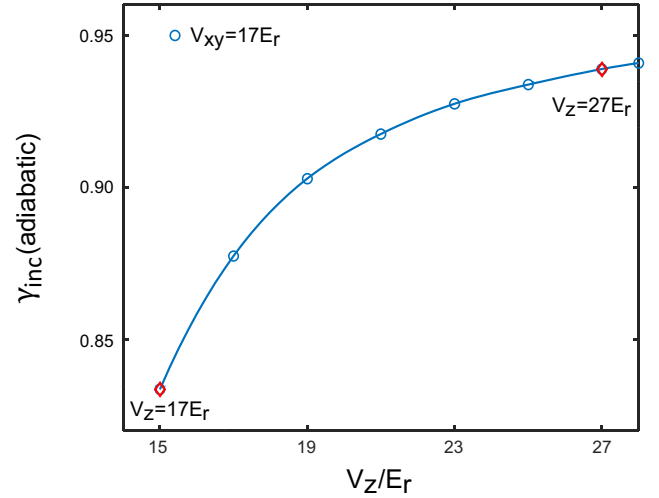
FIG. 5. γ_{inc}(adiabatic) vs V_z at $V_{xy} = 17E_r$. The incoherent fraction increases with V_z, showing the same trend as experiments.

calculate the mean-field terms and a new ground-state wave function. We repeat the overall process, and the energy of states decreases and converges as the iteration increases. We stop the iteration when the energy difference between two adjacent iterations is less than some chosen threshold such as a relative error of 10^{-12}, and the current wave function is approximated as the ground state or the equilibrium state.

The incoherent fraction is defined as

$$\gamma_{\mathrm{inc}} = 1 - \frac{\sum_{i,j}\langle b_i^\dagger \rangle\langle b_j\rangle}{N}, \tag{A3}$$

where $b_i^\dagger$ and b_i are the creation and annihilation operators of site i. To be consistent with the experiment, we simulate a lattice in size of $65 \times 65 \times 65$ sites with particle number $N = 1.5 \times 10^5$, and the allowed maximum filling number is limited to $n = 4$.

First we calculate the incoherent fraction γ_{inc} at $V_{xy} = 17E_r$ with different V_z for the equilibrium states, as shown in Fig. 5. These values correspond to the incoherent fraction γ_{inc}(adiabatic) obtained by the adiabatic ramping. Then we need to consider the dynamical effects and simulate the ramping process by the Runge-Kutta method. In each time step, we need to adjust the chemical potential to keep the particle number unchanged. By starting from the equilibrium states at $V_{xy} = 5E_r$ with different V_z, we increase V_{xy} to $17E_r$ by a certain ramping speed k, which has the same ramping curve as the experiments in the main text. During each time step, we adjust the chemical potential to keep the atom number unchanged. Based on these methods, we obtain how the wave function evolves versus the external ramping. Therefore, we extract out the information of $\gamma_{\mathrm{inc}}(k)$ for these ramping states and calculate the excited defect $n_{\mathrm{ex}} = \gamma_{\mathrm{inc}}$(adiabatic) $- \gamma_{\mathrm{inc}}(k)$.

n_{ex} is the deviation of the ramping states from the equilibrium states, and it describes how many atoms cannot follow the external ramping. Here we will prove that it can be used to describe the excited defects due to the nonadiabatic ramping.

The defect density is defined as [9]

$$n_{\mathrm{defect}} = \langle(\hat{n}_i - \langle\hat{n}_i\rangle)^2\rangle, \tag{A4}$$
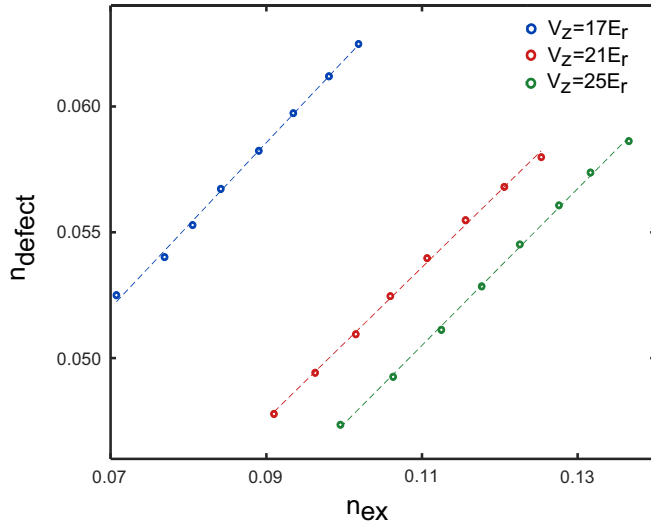
FIG. 6. The defect density n_{defect} vs n_{ex}. We ramp V_{xy} from $5E_r$ to $17E_r$ with different speed k at $V_z = 17E_r$, $21E_r$, and $25E_r$. Then we apply linear fitting on three sets of data to characterize the dependence of n_{ex} on n_{defect}. The hollow circles are GMFT results and the dashed lines are the fitting results. For blue circles, $V_z = 17E_r$ and $n_{\text{defect}} = 0.32(1) \times n_{\text{ex}} + 0.029(4)$. For yellow circles, $V_z = 21E_r$, $n_{\text{defect}} = 0.30(1) \times n_{\text{ex}} + 0.020(6)$. For green circles, $V_z = 25E_r$, $n_{\text{defect}} = 0.31(1) \times n_{\text{ex}} + 0.016(1)$. The slopes are consistent with each other.

where $\hat{n}_i$ is the atom number operator in the lattice site i, $\langle n_i \rangle$ is the mean atom number of the lattice site i, and the outermost brackets $\langle \cdot \rangle$ correspond to the average over all lattice sites (running over all indexes i).

In the deep Mott-insulator regime, the occupation number at each site is fixed and the defect density approaches zero, which, however, is nonzero in the superfluid and the shallow Mott-insulator regimes due to quantum fluctuations. Therefore, n_{defect} of the equilibrium states will be nonzero due to the intrinsic quantum fluctuations. Then, the external ramping introduces additional defects compared with the equilibrium states, and this additional increase in n_{defect} is actually caused by the dynamical excitations. Therefore, our logic is to show the linear dependence between n_{ex} and n_{defect}.

For each V_z with different ramping speed k, we calculate the defect density n_{defect} and compare it with n_{ex}, as shown in Fig. 6. The defect density has a linear dependence on n_{ex} for all sets of V_z, and the slopes of fittings are almost the same. The intercepts of fitting lines are nonzero due to the intrinsic quantum fluctuations of the Mott insulators. When V_z becomes larger, the quantum fluctuations are suppressed and the intercepts decrease. This supports that the observable n_{ex} can serve as the indicator of excited defects.

APPENDIX B: MONTE CARLO WORM ALGORITHM

For Bose-Hubbard models with off-diagonal terms, we use the worm algorithm [43,44,46] to deal with the off-diagonal correlations, and we calculate the Green function at $\tau = 0$. The main idea is to map a d-dimensional quantum system to classical worldlines with $d + 1$ dimension, and then we use the worldlines to describe the system. Here we give a brief introduction to the worldlines and what we do in the calculations.

First, we divide the Bose-Hubbard Hamiltonian into two parts: the diagonal part H^0 and the off-diagonal part H^1 based on the basis of Fock states. Then, the partition function becomes

$$
\begin{aligned}
Z &= \text{Tr}[\exp(-\beta H)] \\
&= \text{Tr}\left[\exp(-\beta H^0) \exp\left(-\int_0^\beta d\tau H^1(\tau) \right) \right],
\end{aligned} \quad \text{(B1)}
$$

where $\beta = 1/T$ and $T \approx 0$ because the atoms are cooled to an ultracold temperature. Rewriting Eq. (B1) as a time-ordered expansion, the mth term is

$$
\int (-1)^m d^m \tau \, e^{-(\beta-\tau_1)H^0_{\alpha_0}} H^1_{\alpha_0, \alpha_1} e^{-(\tau_1-\tau_2)H^0_{\alpha_1}} H^1_{\alpha_{m-1}, \alpha_m} e^{-\tau_m H^0_{\alpha_m}},
$$
$$\text{(B2)}$$

where $\alpha_m = \alpha_0$ guarantees the periodic imaginary-time boundary condition, and the integrals of all τ_i are in the form of path integrals but with imaginary time. Based on this, we decompose the many-body partition functions into summations of all possible path-integral trajectories $W[n_i(\tau)]$. The trajectories $W[n_i(\tau)]$ are based on single-particle representations $n_i(\tau)$, and they are referred to as worldlines. Therefore, the partition function Z is written as

$$
Z = \sum_{n_i(\tau)} W[n_i(\tau)]. \quad \text{(B3)}
$$

Figure 7 shows the typical worldline configuration for partition function Z, which is called the Z-configuration. At one particular imaginary time, the trajectory can hop to a neighboring site due to the off-diagonal term, and then it remains along the imaginary-time axis. All the worldlines start at $\tau = 0$ and end at $\tau = \beta$, which is the most important difference from the G-configuration we are going to introduce below.

To optimize the statistics and calculate the correlation with local updates, the worm algorithm rewrites the Green function by repeating the path-integral procedure above,

$$
G(i_M - i_I, \tau_M - \tau_I) = T_\tau \langle b^\dagger_{i_M}(\tau_M) b_{i_I}(\tau_I) \rangle. \quad \text{(B4)}
$$

The operators $b^\dagger_M$ and b_I claim another particle in the time interval (τ_M, τ_I), adding one more open worldline from point (i_M, τ_M) to (i_I, τ_I), which enlarges the configuration space of the partition function. Following the notation in Refs. [43,46], we call this new configuration space the G-configuration, and the open worldline is defined by a worm pair with a starting point *Masha* and an ending point *Ira*. The properties of an open worldline require $\tau_M \neq 0$ at *Masha* and $\tau_I \neq \beta$ at *Ira*, as shown in Fig. 7.

Under the descriptions of worldlines, we update the system by the worm pair operations. There are four types of operations here: open/close, insert/remove, jump, and move, which have been elaborated on by the previous pioneering works in Refs. [43,46]. Each type of operation corresponds to one possible change of worm pairs. After sufficient sweep times, we achieve the ergodicity of the Green configuration.
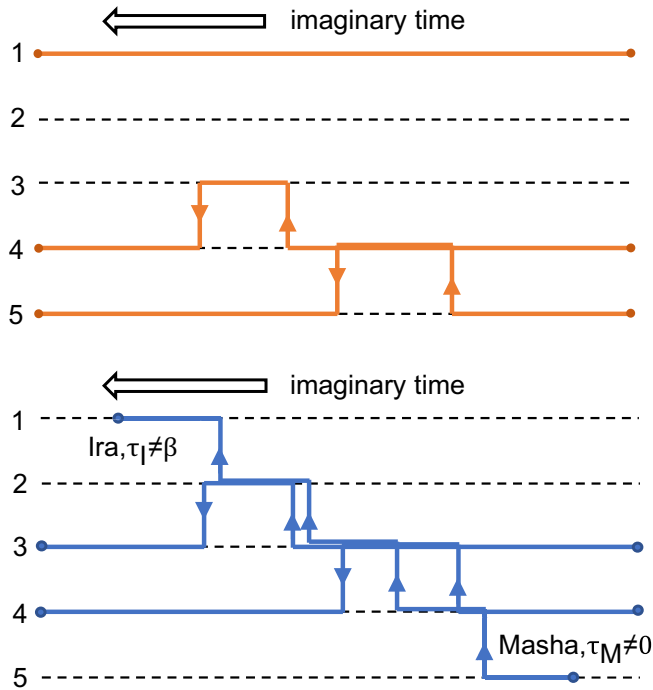
FIG. 7. The Z-configuration (upper panel) and the G-configuration (bottom panel). The Z-configuration contains only closed worldlines, whereas the G-configuration allows open worldlines with Ira ($\tau_I \neq 0$) and Ira ($\tau_M \neq \beta$) at the beginning and end of the worldlines. The update of the system is accomplished by simple operations on the worm pair of $Masha$ and Ira.

FIG. 8. The particle distribution at $V_{xy} = 15E_r$, and $V_z = 15E_r$, $21E_r$, and $27E_r$. We apply two numerical methods to simulate the atom number distribution in the x-y plane with $z = 0$, and r is defined as $\sqrt{x^2 + y^2}$. The smooth lines are the GMFT results, which show consistencies with the zigzag lines by QMC. As V_z gets bigger, the center plateau extends as the incoherent fraction gets larger in the Mott-insulator regime.

The worm algorithm starts with the Z-configuration, and an arbitrary worm pair propagates until the worm head meets the tail in each sweep, walking through all possible paths ergodically. Since the worm pair helps to measure $\langle b_i^\dagger b_j \rangle$, we can calculate the Green functions between different sites.

We perform the worm algorithm on lattices with a size of $65 \times 65 \times 65$ with fixed $V_{xy} = 15E_r$. The maximally allowed occupation number of one site is $n = 3$, and the particle number is $3.3(1) \times 10^3$. At $V_{xy} = 15E_r$ and $V_z \geqslant 13E_r$, the system is in the shallow Mott-insulator regime, allowing us to have a look at the correlation between different layers. We have plotted the results in the main text.

Here we also want to check the effects of limited boundaries. We simulate the particle distribution at the x-y plane centered in the z-direction, as shown in Fig. 8. Ignoring small fluctuations due to limited sweeping times, the QMC result is consistent with the results of GMFT. From the distribution, there are almost no particles at the boundary, hence the limited boundary shows few influences under the chosen parameters.

In the main text, we show the relation between the correlation length and the trap depth along the z-direction at $V_{xy} = 15E_r$, and it exhibits the same trend as t_z/t_{xy}. To illustrate the universality of the results, we plot the correlation lengths for $V_{xy} = 13E_r$, $15E_r$, and $17E_r$, as shown in Fig. 9. At $V_{xy} = 13E_r$ and $V_z = 13E_r$, the correlation length is much larger than one lattice constant, showing the typical correlation in the superfluid. As V_z grows larger, the tunneling between neighboring sites in the z-direction is suppressed,

hence the correlation length decays below one lattice constant a and the system goes into a quasi-2D regime.

APPENDIX C: DEPENDENCE OF TUNNELING AMPLITUDE AND INTERACTION ENERGY ON LATTICE TRAP DEPTH

Here we plot the relations between the tunneling amplitude t_z, the interaction energy U, and the trap depth V_z (Fig. 10). The tunneling amplitude t_z decays stretched-exponentially
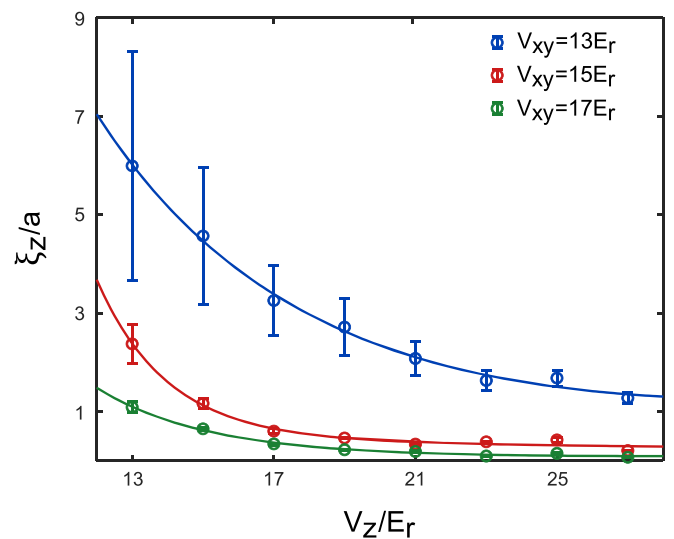
FIG. 9. The correlation length ξ vs V_z at $V_{xy} = 13E_r$, $15E_r$, and $17E_r$. The blue and yellow circles are simulated data for $V_{xy} = 13E_r$, $15E_r$, and $17E_r$, and the corresponding curves are fitted lines. The correlation length ξ decreases as V_{xy} or V_z increases.
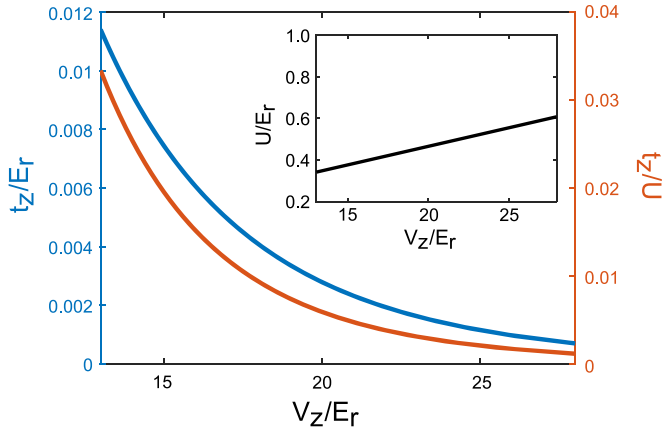
FIG. 10. The tunneling amplitudes t_z and on-site interaction energy U vs trap depth V_z along the z-direction. The blue line with the left axis shows that t_z decays as V_z grows. The red line with the right axis shows the ratio t_z/U. The inset shows U vs V_z.

with the trap depth V_z. The on-site interaction energy U obeys a linear relation with V_z (inset). Compared with t_z, U is almost unchanged while ramping the trap depth. The ratio of t_z and U has the same trend as t_z alone, as shown in the main panel of Fig. 10. Therefore, we use t_z (or t_z/t_{xy}) instead of t_z/U to show the changing trend in the main text, and this helps us to better understand the anisotropy.

APPENDIX D: CALIBRATION OF THE RAMPING ADIABATICITY

To calibrate the ramping adiabaticity, we use a comparison between two ramping curves to see the heating effect during experiments. The time sequences are shown in the inset panels of Fig. 11.

The inset left panel shows a simple ramping that we spend 80 ms to load atoms into the optical lattices with a trap depth $V_i = 10E_r$. Then, we hold atoms for 120 ms and perform the band mapping. The right panel shows that we ramp up the anisotropic lattices with the x-y trap depth $V_f = 17E_r$ and a tunable z trap depth V_z. This costs 80 ms. Then, we hold atoms for 20 ms and ramp down all the lattices into the trap depth $10E_r$ in 80 ms, the same as the trap depth in the left panel.
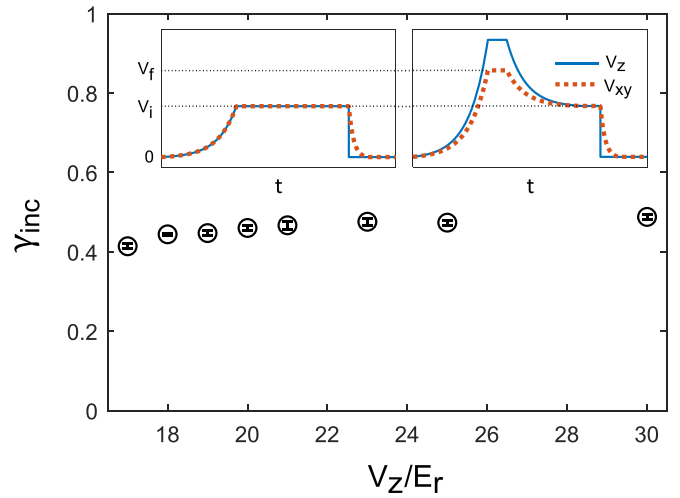
FIG. 11. Calibration of the ramping adiabaticity. The insets show two time sequences of ramping trap depth. The left one is a simple 80 ms ramping to $V_i = 10E_r$ and a 120 ms holding. The right panel is an anisotropic ramping up (80 ms), a holding (20 ms), a ramping down (80 ms), and a holding (20 ms). The main panel shows the measurement results. The red belt shows γ_{inc} in the left inset with one standard deviation. The black dots with error bars (one standard deviation) show γ_{inc} obtained from the right inset.

After the ramp down, we hold atoms for 20 ms and perform the band mapping. This makes the overall time cost of both the left and right inset panels the same.

The data are shown in the same figure (Fig. 11). The red shadow area shows one standard deviation range of the incoherent fraction γ_{inc} in a simple ramping (left inset). The black dots with error bars show the data in the right inset with V_z from $17E_r$ to $30E_r$. The ramping-in and ramping-out increase γ_{inc} by 0.02–0.08 depending on V_z. Our experimental sequence takes half of the time comparing with this measurement. The increase of γ_{inc} is under 0.04, and we think this is small enough for most of the cases.

On the other hand, the heating mainly comes from the changing of V_z, rather than the trap depth in the x-y plane. In the main text, n_{ex} is defined as the difference between two incoherent fractions. Both of them share the same V_z during the preparations, so the heating contributions can be canceled.

[1] T. Giamarchi, *Quantum Physics in One Dimension* (Clarendon Press, Oxford, 2003), Vol. 121.

[2] M. E. Cage, K. Klitzing, A. M. Chang, F. Duncan, M. Haldane, R. B. Laughlin, A. M. M. Pruisken, and D. J. Thouless, *The Quantum Hall Effect* (Springer Science & Business Media, Berlin, 2012).

[3] C. J. Pethick and H. Smith, *Bose-Einstein Condensation in Dilute Gases* (Cambridge University Press, Cambridge, 2008).

[4] A. S. Parkins and D. F. Walls, The physics of trapped dilute-gas Bose-Einstein condensates, Phys. Rep. **303**, 1 (1998).

[5] I. Bloch, J. Dalibard, and W. Zwerger, Many-body physics with ultracold gases, Rev. Mod. Phys. **80**, 885 (2008).

[6] Z. Zhou, X. Zhao, L. Wu, H. Liu, J. Chen, C. Xi, Z. Wang, E. Liu, W. Zhou, S. J. Pennycook, S. T. Pantelides, X.-G. Zhang, L.

Bao, and H.-J. Gao, Dimensional crossover in self-intercalated antiferromagnetic V_5S_8 nanoflakes, Phys. Rev. B **105**, 235433 (2022).

[7] S. Ghosh, W. Bao, D. L. Nika, S. Subrina, E. P. Pokatilov, C. N. Lau, and A. A. Balandin, Dimensional crossover of thermal transport in few-layer graphene, Nat. Mater. **9**, 555 (2010).

[8] C. Liu, Y. Zang, W. Ruan, Y. Gong, K. He, X. Ma, Q.-K. Xue, and Y. Wang, Dimensional Crossover-Induced Topological Hall Effect in a Magnetic Topological Insulator, Phys. Rev. Lett. **119**, 176809 (2017).

[9] D. Pekker, B. Wunsch, T. Kitagawa, E. Manousakis, A. S. Sørensen, and E. Demler, Signatures of the superfluid to Mott insulator transition in equilibrium and in dynamical ramps, Phys. Rev. B **86**, 144527 (2012).

[10] M. P. A. Fisher, P. B. Weichman, G. Grinstein, and D. S. Fisher, Boson localization and the superfluid-insulator transition, Phys. Rev. B **40**, 546 (1989).

[11] A. Polkovnikov, Universal adiabatic dynamics in the vicinity of a quantum critical point, Phys. Rev. B **72**, 161201(R) (2005).

[12] B. D. Josephson, Inequality for the specific heat: I. derivation, Proc. Phys. Soc. **92**, 269 (1967).

[13] A. D. Sokal, More inequalities for critical exponents, J. Stat. Phys. **25**, 25 (1981).

[14] T. W. B. Kibble, Topology of cosmic domains and strings, J. Phys. A **9**, 1387 (1976).

[15] W. H. Zurek, Cosmological experiments in superfluid helium? Nature (London) **317**, 505 (1985).

[16] P. Silvi, G. Morigi, T. Calarco, and S. Montangero, Crossover from Classical to Quantum Kibble-Zurek Scaling, Phys. Rev. Lett. **116**, 225701 (2016).

[17] S. Braun, M. Friesdorf, S. S. Hodgman, M. Schreiber, J. P. Ronzheimer, A. Riera, M. Del Rey, I. Bloch, J. Eisert, and U. Schneider, Emergence of coherence and the dynamics of quantum phase transitions, Proc. Natl. Acad. Sci. USA **112**, 3641 (2015).

[18] L. W. Clark, L. Feng, and C. Chin, Universal space-time scaling symmetry in the dynamics of bosons across a quantum phase transition, Science **354**, 606 (2016).

[19] A. Keesling, A. Omran, H. Levine, H. Bernien, H. Pichler, S. Choi, R. Samajdar, S. Schwartz, P. Silvi, S. Sachdev, P. Zoller, M. Endres, M. Greiner, V. Vuletić, and M. D. Lukin, Quantum Kibble-Zurek mechanism and critical dynamics on a programmable Rydberg simulator, Nature (London) **568**, 207 (2019).

[20] J. Goo, Y. Lim, and Y.-I. Shin, Defect Saturation in a Rapidly Quenched Bose Gas, Phys. Rev. Lett. **127**, 115701 (2021).

[21] X.-P. Liu, X.-C. Yao, Y. Deng, Y.-X. Wang, X.-Q. Wang, X. Li, Q. Chen, Y.-A. Chen, and J.-W. Pan, Dynamic formation of quasicondensate and spontaneous vortices in a strongly interacting Fermi gas, Phys. Rev. Res. **3**, 043115 (2021).

[22] Q. Huang, R. Yao, L. Liang, S. Wang, Q. Zheng, D. Li, W. Xiong, X. Zhou, W. Chen, X. Chen, and J. Hu, Observation of Many-Body Quantum Phase Transitions beyond the Kibble-Zurek Mechanism, Phys. Rev. Lett. **127**, 200601 (2021).

[23] L. Liang, W. Zheng, R. Yao, Q. Zheng, Z. Yao, T.-G. Zhou, Q. Huang, Z. Zhang, J. Ye, X. Zhou, X. Chen, W. Chen, H. Zhai, and J. Hu, Probing quantum many-body correlations by universal ramping dynamics, Sci. Bull. **67**, 2550 (2022).

[24] K.-S. Ryu, H. Akinaga, and S.-C. Shin, Tunable scaling behaviour observed in Barkhausen criticality of a ferromagnetic film, Nat. Phys. **3**, 547 (2007).

[25] J. P. Sethna, Crackling crossover, Nat. Phys. **3**, 518 (2007).

[26] Y. J. Chen, S. Zapperi, and J. P. Sethna, Crossover behavior in interface depinning, Phys. Rev. E **92**, 022146 (2015).

[27] H. C. Chauhan, B. Kumar, A. Tiwari, J. K. Tiwari, and S. Ghosh, Different Critical Exponents on Two Sides of a Transition: Observation of Crossover From Ising to Heisenberg Exchange in Skyrmion Host Cu_2OSeO_3, Phys. Rev. Lett. **128**, 015703 (2022).

[28] P. V. Prudnikov, V. V. Prudnikov, M. A. Menshikova, and N. I. Piskunova, Dimensionality crossover in critical behaviour of ultrathin ferromagnetic films, J. Magn. Magn. Mater. **387**, 77 (2015).

[29] M. P. McDonald, R. Chatterjee, J. Si, B. Jankó, and M. Kuno, Dimensional crossover in semiconductor nanostructures, Nat. Commun. **7**, 12726 (2016).

[30] A. V. Chalyi, Dimensional crossover in liquids in reduced geometry, in *Physics of Liquid Matter: Modern Problems* (Springer International Publishing, Berlin, 2015), pp. 31–49.

[31] Á. Pásztor, A. Scarfato, C. Barreteau, E. Giannini, and C. Renner, Dimensional crossover of the charge density wave transition in thin exfoliated VSe_2, 2D Mater. **4**, 041005 (2017).

[32] D. A. Egolf and H. S. Greenside, Relation between fractal dimension and spatial correlation length for extensive chaos, Nature (London) **369**, 129 (1994).

[33] L. Chomaz, L. Corman, T. Bienaimé, R. Desbuquois, C. Weitenberg, S. Nascimbene, J. Beugnon, and J. Dalibard, Emergence of coherence via transverse condensation in a uniform quasi-two-dimensional Bose gas, Nat. Commun. **6**, 6162 (2015).

[34] E. Ibarra-García-Padilla, R. Mukherjee, R. G. Hulet, K. R. A. Hazzard, T. Paiva, and R. T. Scalettar, Thermodynamics and magnetism in the two-dimensional to three-dimensional crossover of the Hubbard model, Phys. Rev. A **102**, 033340 (2020).

[35] H. Lee, S. Fang, and D.-W. Wang, Quantitative studies of the critical regime near the superfluid-to-Mott-insulator transition, Phys. Rev. A **95**, 053622 (2017).

[36] U. Toniolo, B. C. Mulkerin, C. J. Vale, X.-J. Liu, and H. Hu, Dimensional crossover in a strongly interacting ultracold atomic Fermi gas, Phys. Rev. A **96**, 041604(R) (2017).

[37] X. Zhang, C.-L. Hung, S.-K. Tung, and C. Chin, Observation of quantum criticality with ultracold atoms in optical lattices, Science **335**, 1070 (2012).

[38] A. Bermudez, D. Patane, L. Amico, and M. A. Martin-Delgado, Topology-Induced Anomalous Defect Production by Crossing a Quantum Critical Point, Phys. Rev. Lett. **102**, 135702 (2009).

[39] A. Bermudez, L. Amico, and M. A. Martin-Delgado, Dynamical delocalization of Majorana edge states by sweeping across a quantum critical point, New J. Phys. **12**, 055014 (2010).

[40] D. S. Rokhsar and B. G. Kotliar, Gutzwiller projection for bosons, Phys. Rev. B **44**, 10328 (1991).

[41] D. Jaksch, C. Bruder, J. I. Cirac, C. W. Gardiner, and P. Zoller, Cold Bosonic Atoms in Optical Lattices, Phys. Rev. Lett. **81**, 3108 (1998).

[42] J. Zakrzewski, Mean-field dynamics of the superfluid-insulator phase transition in a gas of ultracold atoms, Phys. Rev. A **71**, 043601 (2005).

[43] N. Prokof'ev and B. Svistunov, Worm algorithm for problems of quantum and classical statistics, in *Understanding Quantum Phase Transitions*, edited by L. Carr (Taylor & Francis, Boca Raton, FL, 2010), pp. 499–522.

[44] V. A. Kashurnikov, N. V. Prokof'Ev, and B. V. Svistunov, Revealing superfluid-Mott-insulator transition in an optical lattice, Phys. Rev. A **66**, 031601 (2002).

[45] M. B. Hastings and T. Koma, Spectral gap and exponential decay of correlations, Commun. Math. Phys. **265**, 781 (2006).

[46] N. V. Prokof'Ev, B. V. Svistunov, and I. S. Tupitsyn, Exact, complete, and universal continuous-time worldline Monte Carlo approach to the statistics of discrete quantum systems, J. Exp. Theor. Phys. **87**, 310 (1998).